

E. JMA-RATM¹

E-1. Original and Preliminary RATM

E-1-1. Description of RATM

The JMA-RATM (Japan Meteorological Agency Regional Atmospheric Transport Model, called the ‘RATM’ in this chapter) is a mesoscale tracer transport model, which can be driven by the JMA-MESO analysis GPVs (grid point values). The model takes a Lagrangian scheme (Iwasaki et al., 1998; Seino et al., 2004) with many computational particles that follow advection, horizontal and vertical diffusion, gravitational settling, wet scavenging and dry deposition processes. The RATM was originally developed at JMA for photochemical oxidant predictions (Takano et al., 2007) and volcanic-ash fall forecasts (Shimbori et al., 2009). In this section, we describe the original version of RATM (Shimbori et al., 2010) and a preliminary version of RATM to simulate radionuclides for the WMO technical Task Team (Saito et al., 2015). Flowchart of the RATM calculation for radionuclides is shown in Fig. E-1-1. Specifications of each version of the RATM are summarized in Table E-1-1.

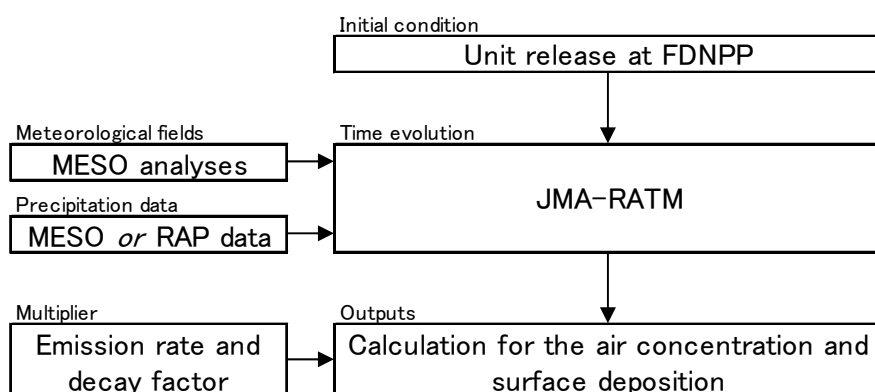


Fig. E-1-1. Flowchart of the JMA-RATM calculation for radionuclides.

a. Advection

We write the position $(x(t), y(t), z(t))$ for each computational particle at time t . The time evolution after the time step Δt is given by

$$x(t + \Delta t) = x(t) + \overline{u(t)}\Delta t + u'(t)\Delta t \quad (\text{E-1-1a})$$

$$y(t + \Delta t) = y(t) + \overline{v(t)}\Delta t + v'(t)\Delta t \quad (\text{E-1-1b})$$

$$z(t + \Delta t) = z(t) + \overline{w(t)}\Delta t + \sqrt{2K_v\Delta t}\Gamma - V_t\Delta t \quad (\text{E-1-1c})$$

with the mean wind velocity $(\overline{u(t)}, \overline{v(t)}, \overline{w(t)})$. On the right-hand sides of above equations, the second and third terms represent advection and diffusion, respectively. The fourth term of Eq. (E-1-1c) represents gravitational settling.

¹ T. Shimbori and K. Saito

Table E-1-1. Specifications of JMA-RATM.

| Version | | Original | Preliminary | Revised | | Test |
|---|------------------------------------|--|--|--|---|---|
| | | for JMA Volcanic Ash Fall Forecast ¹ | for WMO Task Team | | for SCJ Working Group | |
| Model type | | Lagrangian description | | | | |
| Input meteorological field | | Hourly outputs of MESO forecast GPVs | Three-hourly outputs of MESO analysis GPVs | | | |
| Number of particles | | 100,000/10 min. | 100,000/3 h | 300,000/3 h | | |
| Time step | | 3 min. | 10 min. | | 5 min. | |
| Advection | Horizontal | Forward difference with spherical triangle | | | | |
| | Vertical | Not adjusted | | Spatially-average and terrain-following at lowest model level | | |
| Horizontal diffusion | | Gifford (1982, 1984) | | | | |
| Vertical diffusion | | Louis et al. (1982) | | | | |
| Gravitational settling ² (grain-size distribution) | | Vpar: Suzuki (1983) (log-normal with $D_m=0.25$ mm, $\sigma_D=1.0$) | Ngas: N/A Dgas: N/A Lpar: Stokes' law with Cunningham correction (log-normal with $D_m=1$ μ m, $\sigma_D=1.0$) | | | |
| Wet scavenging ² | Washout ³ (below-cloud) | Vpar: Kitada (1994) with MESO forecast (liquid rain) | Ngas: N/A Dgas: N/A Lpar: Kitada (1994) with MESO analysis (liquid rain) or RAP data below 3000 m a.s.l. | Ngas: N/A Dgas: N/A Lpar: same as left except application height below 1500 m a.s.l. | Ngas: N/A Dgas: N/A Lpar: same as left except using MESO analysis (liquid rain, solid snow and graupel) | |
| | Rainout (in-cloud) | Vpar: N/A | Ngas: N/A Dgas: Hertel et al. (1995) Lpar: N/A | | | Ngas: N/A Dgas: same as left Lpar: Hertel et al. (1995) |
| Dry-deposition ² | | Vpar: $V_d=0.3$ m s ⁻¹ (Shao, 2000) | Ngas: N/A Dgas: $V_d=0.01$ m s ⁻¹ (Draxler and Rolph, 2012) Lpar: $V_d=0.001$ m s ⁻¹ (Draxler and Rolph, 2012) | | | |
| Reflection on the ground | | N/A | Iwasaki et al. (1998) | | | |
| Radioactive decay | | N/A | Half-lifetime | | | |
| Output grid size | | 5 km | | | | |
| References | | Shimbori et al. (2010) | Draxler et al. (2013a), Saito et al. (2015) | | Takigawa et al. (2013), Saito et al. (2015), SCJ (2014) | Saito et al. (2015) |

¹ As of March 2011. JMA-RATM for volcanic ash was replaced on March 2013 (Shimbori et al., 2014).

² The abbreviations Ngas, Dgas, Lpar and Vpar mean noble gas, depositing gas, light aerosol and volcanic-ash particle, respectively.

³ Below-scavenging coefficients Λ_w are listed in Table E-3-4.

b. Horizontal diffusion

Under the assumption of horizontally homogeneous turbulence, the x - and y -components of subgrid-scale turbulent velocity in Eqs. (E-1-1a) and (E-1-1b) are given by Uliasz (1990):

$$u'(t) = R_h(\Delta t)u'(t - \Delta t) + \sqrt{1 - R_h(\Delta t)^2}\sigma_{u'}\Gamma \quad (\text{E-1-2a})$$

$$v'(t) = R_h(\Delta t)v'(t - \Delta t) + \sqrt{1 - R_h(\Delta t)^2}\sigma_{v'}\Gamma \quad (\text{E-1-2b})$$

with the initial conditions $u'(0) = u'_0\Gamma$ and $v'(0) = v'_0\Gamma$. The u'_0 and v'_0 are the magnitudes of turbulent horizontal velocities at the emission point and Γ is a normal random number with mean 0 and variance 1. R_h is the Lagrangian autocorrelation function of the turbulent velocity represented by

$$R_h(\Delta t) = e^{-\Delta t/t_{Lh}} \quad (\text{E-1-3})$$

with Lagrangian time scale t_{Lh} . $\sigma_{u'}$ and $\sigma_{v'}$ are the standard deviations of u' and v' , respectively, given by

$$\sigma_{u'}^2 \approx \sigma_{v'}^2 = \frac{K_h}{t_{Lh}} \quad (\text{E-1-4})$$

with the horizontal diffusion coefficient K_h for $t \gg t_{Lh}$. Substituting Eqs. (E-1-3) and (E-1-4) into (E-1-2a) and (E-1-2b), to the first order in Δt , we obtain the Langevin equation. Then the horizontal diffusion scheme represented by Eqs. (E-1-2a) and (E-1-2b) is the analogue of Brownian motion (Gifford, 1982, 1984).

For the three parameters in Eqs. (E-1-2a), (E-1-2b) - (E-1-4), we set as $u'_0 = 0.253 \text{ m s}^{-1}$, $t_{Lh} = 5.0 \times 10^4 \text{ s}$ and $K_h = 5.864 \times 10^4 \text{ m}^2 \text{ s}^{-1}$ according to Kawai (2002).

c. Vertical diffusion

The vertical diffusion coefficient in the third term on the right-hand side of Eq. (E-1-1c) are determined by Louis et al. (1982):

$$K_v = l^2 \left| \frac{\partial \bar{U}}{\partial z} \right| F_v(R_f) \quad (\text{E-1-5})$$

where l is the mixing length in an analogy to the mean free path in molecular diffusion, \bar{U} is the mean horizontal wind velocity, and $F_v(R_f)$ representing atmospheric stability is a function of flux

Richardson number R_f given by the level 2 scheme of Mellor and Yamada (1974, 1982). The mixing length takes the form (Blackadar, 1962)

$$l = \frac{kz}{1 + kz/l_0} \quad (\text{E-1-6})$$

where k is the Kármán constant (≈ 0.4), z is height from ground surface and l_0 is maximum mixing length [m] given by Holtslag and Boville (1993):

$$l_0 = \begin{cases} 30 + 70 \exp\left(1 - \frac{z}{1000}\right), & z > 1000 \text{ m} \\ 100, & z \leq 1000 \text{ m} \end{cases} \quad (\text{E-1-7})$$

The upper limit of K_v is set to $50 \text{ m}^2 \text{ s}^{-1}$ according to Yamazawa et al. (1998).

The above-mentioned schemes of advection and diffusion are used in original RATM and are also applied to radionuclides in the preliminary and revised RATM.

d. Gravitational settling

For dealing with light particles (Lpar) of radionuclides, i.e. radioactive matter or other accumulation-mode aerosol particles carrying some radioactive matter (e.g. ^{137}Cs), gravitational settling follows Stokes' law with a slip correction and the terminal velocity is given by (e.g., Sportisse, 2007)

$$V_t(D, z) = \frac{1}{18} \frac{\rho_p g D^2}{\eta_a / C_c} \quad (\text{E-1-8})$$

where C_c is the Cunningham correction factor

$$C_c = 1 + Kn \left[a + b \exp\left(-\frac{c}{Kn}\right) \right], a = 1.257, b = 0.400, c = 1.100 \quad (\text{E-1-9})$$

with the Knudsen number $Kn \equiv 2\lambda_a/D$. The viscosity η_a and the mean free path λ_a of air are calculated by

$$\eta_a(z) = \eta_0 \left[\frac{T_0 + C_s}{T_a(z) + C_s} \right] \left[\frac{T_a(z)}{T_0} \right]^{3/2} \quad (\text{E-1-10})$$

$$\lambda_a(z) = \lambda_0 \frac{\eta_a(z)}{\eta_0} \left[\frac{p_a(z)}{p_0} \right]^{-1} \left[\frac{T_a(z)}{T_0} \right]^{1/2} = \lambda_0 \left[\frac{p_a(z)}{p_0} \right]^{-1} \left[\frac{T_0 + C_s}{T_a(z) + C_s} \right] \left[\frac{T_a(z)}{T_0} \right]^2 \quad (\text{E-1-11})$$

where p_a the air pressure, T_a the air temperature, C_S the Sutherland constant of air (=117 K) and $\eta_0 = 18.2 \mu\text{Pa s}$, $\lambda_0 = 0.0662 \mu\text{m}$ are the standard values for the reference atmosphere ($T_0 = 293.15 \text{ K}$, $p_0 = 1013.25 \text{ hPa}$). The distribution of particle size D is assumed to be log-normal with mean diameter $D_m = 1 \mu\text{m}$ and standard deviation $\sigma_D = 1.0$ (upper cutoff: $20 \mu\text{m}$). The particle density ρ_p is 1 g cm^{-3} for all particle sizes.

Note that if a computational particle moves under the model surface by the vertical motion, it is numerically reflected to the mirror symmetric point above the surface.

e. Wet scavenging

(1) Washout (below-cloud scavenging)

Because the original RATM was not applied in predicting the dispersion and deposition of radionuclides, the wet scavenging schemes needed to be modified for this application. For Lpar, based on the original treatment of wet scavenging, only washout processes (below-cloud scavenging) are considered. The below-cloud scavenging rate by rain (liquid water) is given by Kitada (1994) (red solid line of Fig. E-1-2):

$$\Lambda_w = AP^B \quad (\text{E-1-12})$$

$$A = 2.98 \times 10^{-5} (\text{s}^{-1}), B = 0.75 \quad (\text{E-1-13})$$

where P is the precipitation intensity [mm h^{-1}].

(2) Rainout (in-cloud scavenging)

On the other hand, wet deposition for a depositing gas (Dgas, e.g. ^{131}I) is considered only as a rainout process (in-cloud scavenging). The in-cloud scavenging rate for Dgas is given by Hertel et al. (1995):

$$\Lambda_r = \frac{1}{(1 - LWC)/HRT_a + LWC Z_r} \frac{P}{Z_r} [\text{h}^{-1}] \quad (\text{E-1-14})$$

where LWC the liquid water content, H the Henry constant ($=0.08 \text{ M atm}^{-1}$; Sect. F-1), R the ideal-gas constant ($=0.082 \text{ atm M}^{-1} \text{ K}^{-1}$), and Z_r the height over which in-cloud scavenging takes place.

Wet scavenging is applied to Lpar or Dgas under the height of about 3000 m a.s.l. in the original and preliminary RATM (Shimbori et al. 2010). In the case of in-cloud scavenging for Dgas, however, we have not been able to calibrate the RATM results. Therefore the Sect. E-3 results are devoted to Lpar (^{137}Cs and particulate ^{131}I) verification.

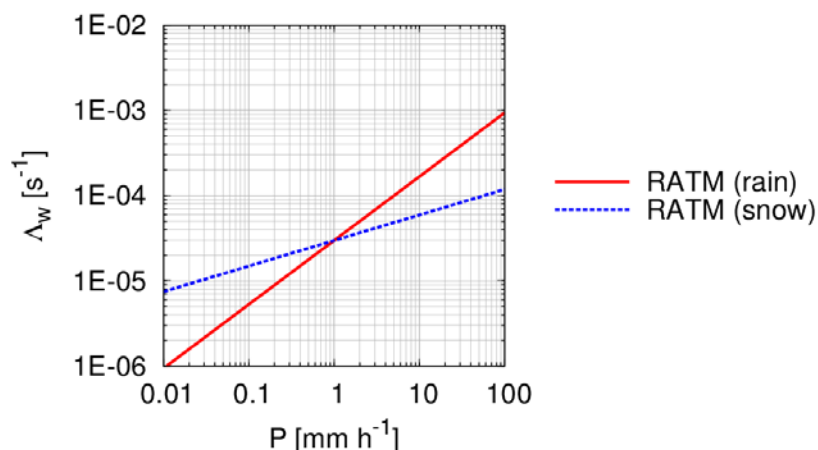


Fig. E-1-2. Below-cloud scavenging coefficients for rain (red solid line) and snow and graupel (blue dotted line) used in JMA-RATM. After Saito et al. (2015).

f. Dry deposition

Dry deposition is simply computed from the following deposition rate (e.g., Iwasaki et al., 1998):

$$\Lambda_d = \frac{V_d}{Z_d} \quad (\text{E-1-15})$$

where V_d is the dry-deposition velocity and Z_d is the depth of surface layer. The value of V_d is set to 0.001 m s^{-1} for Lpar and 0.01 m s^{-1} for Dgas (Sportisse, 2007; Draxler and Rolph, 2012), and Z_d is set to 100 m for both tracer types.

E-1-2. Use of MESO GPVs and RAP data

In Fig. E-1-1, the motion of computational particles in RATM is calculated in the same coordinate system as the MESO analysis (Lambert conformal mapping in the horizontal and a terrain-following hybrid in the vertical). The three-hourly 5-km MESO GPV data used to drive the RATM are momentum, potential temperature, pressure, density, accumulated precipitation and mixing ratio of cloud water. In the advection and diffusion steps, the mean wind velocities at each computational particle are calculated from the time-space interpolation of the density and momentum GPVs. To calculate the settling velocity, the temperature and pressure GPVs are used. For the wet scavenging process, the precipitation intensity is computed from the average of the three-hour accumulated precipitation GPVs. *LWC* for the in-cloud scavenging computation can be defined by the GPVs of mixing ratio of cloud water. However, due to limitations in the treatment of ice-phase deposition in the original RATM, only liquid rain was considered in the WMO Task Team calculation. Subsequently, we used the total precipitation in the SCJ (Science Council of Japan) Working Group calculations.

When using the RAP data, instead of the three-hourly accumulated precipitation by MESO GPVs, the RAP intensity at each MESO grid point (5-km resolution) is calculated from the spatial average of the surrounding 25-grid cells of RAP (1-km resolution) every 30 min. As noted above, because the original version of RATM cannot treat ice-phase deposition and RAP data do not distinguish solid and liquid precipitations, all RAP data were considered to be liquid rain in the calculation.

E-2. Revision of RATM²

As previously mentioned in Sect. B-3-2, the JMA-MESO analysis is produced by a three-hour forecast of the 5-km outer-loop of JMA-NHM (Saito et al., 2006, 2007, 2012) of JNoVA (Honda et al., 2005; Honda and Sawada, 2008). The stored values in the analysis field are not averaged in the assimilation window but are the instantaneous values predicted by the outer-loop model at the analysis time (the end of each three-hour assimilation window). Because the instantaneous vertical motion is affected by gravity waves and short-lived convection, a simple time interpolation of updrafts/downdrafts between the three-hourly analysis fields may yield an overestimation of the vertical advection of the air parcel, even if the magnitude of updrafts/downdrafts is small.

To compensate for the lack of temporal resolution, in the revised version of JMA-RATM, the vertical advection (the second term on the right-hand side of Eq. (E-1-1c)) is calculated using a spatially-averaged (nine-grid cells) value of the MESO vertical velocity and assumed to be terrain-following ($w(z^* = 40 \text{ m}) = 0$) at the lowest model level. Figure E-2-1 compares the 24-h Lpar accumulated deposition for unit release (1 Bq/h) from 0000 UTC to 0300 UTC 14 March 2011. The upper-right panel shows the result where vertical motion of the particles is computed using the original MESO vertical velocity. Compared to the case without vertical advection (upper-left panel), the deposition over the sea off the east coast of Japan is reduced. The lower-left panel provides the result when the nine-grid cell averaged updraft/downdraft was applied to compute the vertical advection. The difference from the upper-right panel is not large but the deposition is slightly increased near the FDNPP (Fukushima Daiichi Nuclear Power Plant) site and slightly decreased at distant areas. In these simulations, Lpar emitted from the FDNPP site were first lifted up by the lowest level's small updraft in MESO GPVs. The lower-right panel is the result of when the lowest level vertical motion was assumed to be terrain following (i.e., the lowest level updraft/downdraft becomes zero over sea while the remaining vertical motion over land is just due to the terrain slope and the horizontal wind speed). The deposition off the east coast of Japan is increased.

In the preliminary version of RATM, wet scavenging was assumed to occur below about 3000 m in height, the same as in the original RATM (Table E-1-1), but deposition over Miyagi prefecture, to the north of Fukushima, was overestimated compared with the aircraft monitoring by the MEXT (Sect. D-3). In the revised RATM, this overestimation was reduced by limiting the level of wet scavenging to levels below about 1500 m (see Sect. E-3).

Some improper treatments of horizontal and vertical interpolations of the kinematic fields were found in the preliminary version of RATM. These computational bugs were corrected in the revised version. Also the number of computational particles was increased from 100,000/3 h to 300,000/3 h, but the impact was almost negligible (see Sect. E-3).

For the model intercomparison of the SCJ Working Group, we further modified RATM as noted previously: the time step was changed from 10 min. to 5 min. and in addition to rain, the precipitation

² The description is based on Sect. 3 of Saito et al. (2015).

intensity of snow and graupel in the MESO GPVs was used. For these calculations, the below-cloud scavenging coefficients of L_{par} in Eq. (E-1-12) for snow and graupel are assumed (blue dotted line of Fig. E-1-2)

$$A = 2.98 \times 10^{-5} \text{ (s}^{-1}\text{)}, B = 0.30 \quad (\text{E-2-1})$$

with reference to the B value of UKMET-NAME (Table F-2-1). The impacts of the modifications are shown in next section.

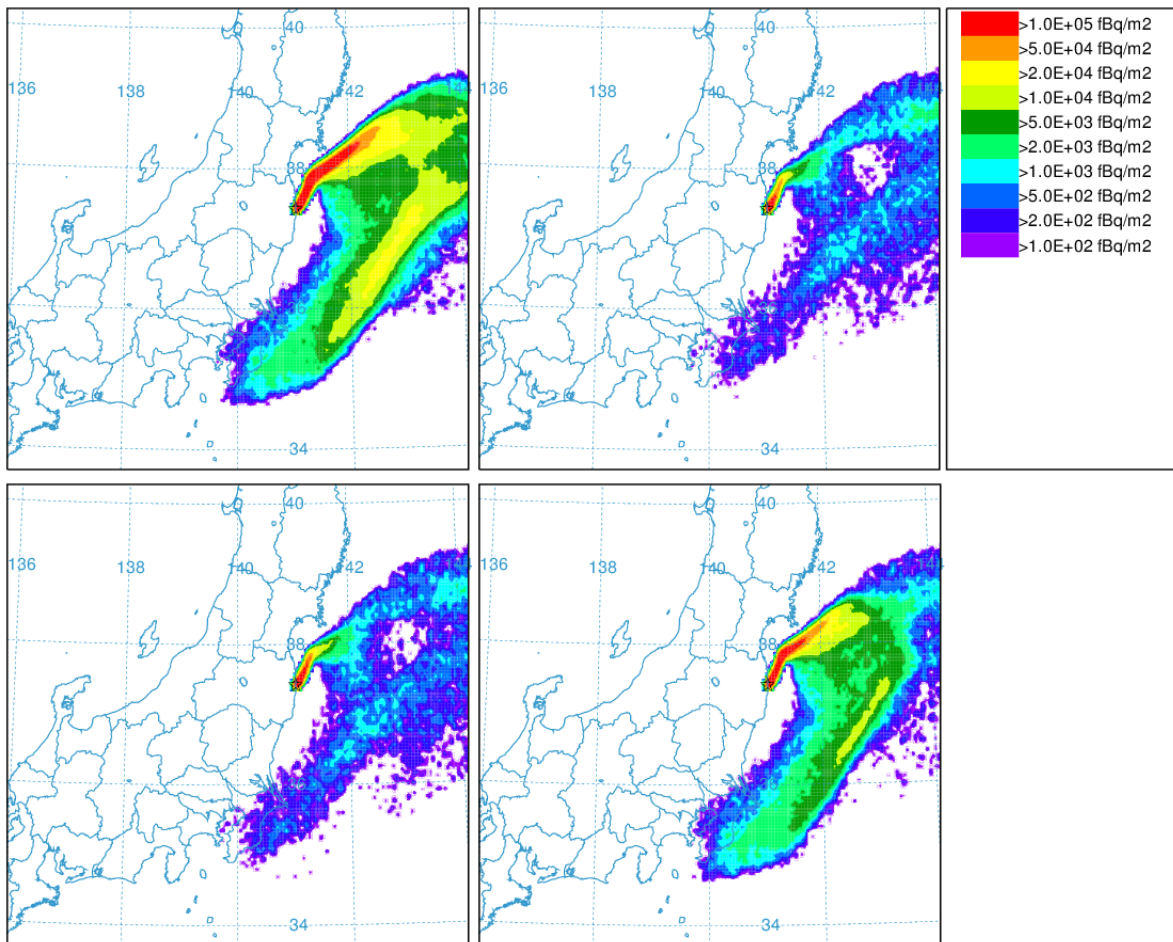


Fig. E-2-1. 24-h L_{par} accumulated deposition by the JMA-RATM for unit release (1 Bq/h) at 0000-0300 UTC 14 March 2011. JMA-MESO GPV is used for precipitation. Upper left: without vertical advection. Upper right: vertical motion is computed by updraft/downdraft. Lower left: spatially-average is applied. Lower right: spatially-average and terrain-following at the lowest level. Star symbols indicate the location of FDNPP. These deposition maps are created by the drawing tool of the NOAA ARL website (Sect. D-4). After Saito et al. (2015).

E-3. Experiments with RATM³

E-3-1. Comparison with preliminary and revised RATM for the WMO Task Team

a. Experimental setting

According to the computational design described in Sect. D-1, JMA-RATM simulations were conducted by the WMO Task Team for the computational period of 1800 UTC 11 March through 2400 UTC 31 March, in three-hourly emission period increments using a unit source rate (1 Bq/h) for each discrete emission time segment. Emissions were uniformly distributed from the ground surface to 100 m a.g.l., and the concentration or deposition at any grid cell in the domain was given by the sum of the contribution from all the RATM emission segments after multiplying the resulting unit concentrations by the emission rate for each segment (Sect. D-1). The air concentration and deposition output fields were configured to use a regular latitude-longitude grid (601 by 401 grid cells) with the output averaged at three-hourly intervals at 0.05° (5 km) horizontal resolution and 100 m vertical resolution. In the post-processing step, the results from each of the 168 RATM simulations were multiplied by the actual emission rate at the release time of the simulation and decay constant for each radionuclide thereby permitting the RATM dispersion and deposition factors to be applied to multiple radionuclides. The estimated emission rates ‘JAEA’ (red solid line in Fig. 2 of Draxler et al. (2015)), originally derived by Chino et al. (2011) and later modified by Terada et al. (2012, in Sect. D-2) were used for the WMO Task Team simulations.

Figure E-3-1 compares ¹³⁷Cs accumulated deposition for 11 March to 3 April 2011 estimated using different computational methodologies. Here, rain in MESO GPVs was used for the calculations shown in the left panels while RAP data were used for those shown in the right panels. In the preliminary RATM (upper figures), deposition over Miyagi prefecture (north of Fukushima) and southern part of the Kanto Plain (west of Tokyo) was overestimated compared with observation as mentioned in the previous section E-2. In the revised RATM (lower figures), this overestimation was ameliorated. When RAP data is used for precipitation, an area with high deposition in the northwest of FDNPP becomes more distinctly reproduced (right figures), but the overestimation of deposition in the southern part of the Kanto Plain is also enhanced, even in the revised RATM.

b. Verifications against observation

The ¹³⁷Cs dispersion and deposition were verified against the observed time series of near ground level air concentrations at JAEA-Tokai (see Sect. D-2) and the deposition measurements taken by aerial and ground based sampling (Fig. D-3-1 in Sect. D-3). One of the characteristic features of the deposition pattern is the densely contaminated area extending to northwest from FDNPP. This area is bent to the south, east of Ou mountain range, and forms an inverse L-shaped pattern shown by the yellow shaded region in Fig. D-3-1. On the other hand, deposition in Miyagi prefecture, north of Fukushima, is relatively small.

³ The description is based on Sects. 4 and 5 of Saito et al. (2015).

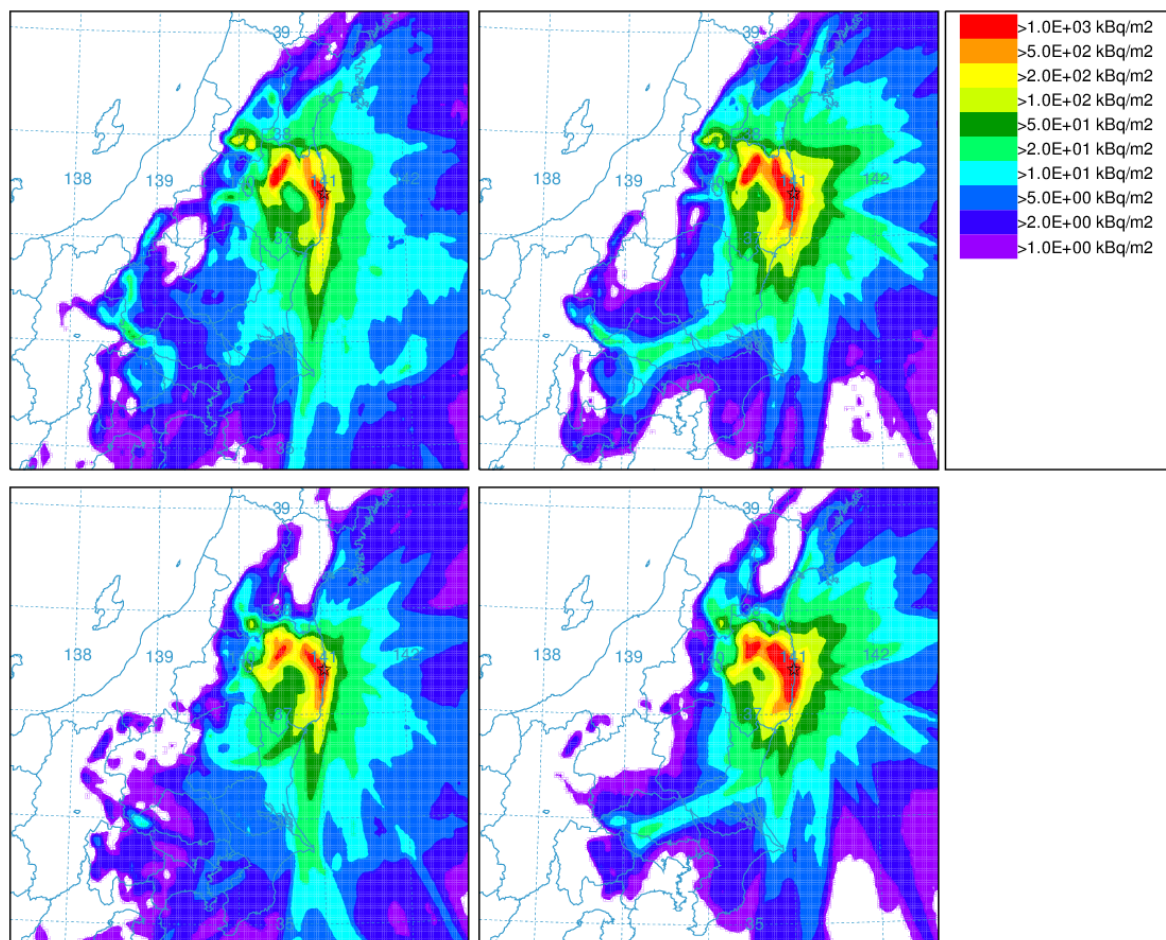


Fig. E-3-1. ^{137}Cs accumulated deposition for 11 March-3 April 2011 using the JAEA source. Upper left: preliminary RATM with MESO precipitation. Upper right: preliminary RATM with RAP precipitation. Lower: same as in upper panels but results by the revised RATM. After Saito et al. (2015).

The statistics of correlation coefficient ($-1 \leq R \leq 1$), fractional bias ($-2 \leq \text{FB} \leq 2$), figure-of-merit in space (FMS [%]), Kolmogorov-Smirnov parameter (KSP [%]) mentioned in Sect. D-3 and the following two additional statistics used in Draxler et al. (2013a) were applied to the results of the preliminary and revised RATM.

- i) Factor of two percentage (FA2 [%]), the percentage of calculations within a factor of two of the measured value.
- ii) Factor of exceedance ($-50\% \leq \text{FOEX} \leq 50\%$), the factor of the number of over-predictions in the pairs of predicted and measured values.

A ranking method was defined by giving equal weight to the normalized expressions of these statistics (Draxler et al., 2013a),

$$\text{METRIC1} \equiv \text{Rank} = R^2 + 1 - \left| \frac{\text{FB}}{2} \right| + \frac{\text{FMS}}{100} + \left(1 - \frac{\text{KSP}}{100} \right) \quad (\text{E-3-1a})$$

$$\text{METRIC2} = R^2 + 1 - \left| \frac{\text{FB}}{2} \right| + \frac{\text{FA2}}{100} + \left(1 - \frac{\text{KSP}}{100} \right) \quad (\text{E-3-1b})$$

$$\begin{aligned} \text{METRIC3} &= \text{METRIC1} + \left(1 - \left|\frac{\text{FOEX}}{50}\right|\right) \\ &= R^2 + 1 - \left|\frac{\text{FB}}{2}\right| + \frac{\text{FMS}}{100} + \left(1 - \left|\frac{\text{FOEX}}{50}\right|\right) + \left(1 - \frac{\text{KSP}}{100}\right) \end{aligned} \quad (\text{E-3-1c})$$

$$\begin{aligned} \text{METRIC4} &= \text{METRIC3} + \text{FA2}/100 \\ &= R^2 + 1 - \left|\frac{\text{FB}}{2}\right| + \frac{\text{FMS}}{100} + \frac{\text{FA2}}{100} + \left(1 - \left|\frac{\text{FOEX}}{50}\right|\right) + \left(1 - \frac{\text{KSP}}{100}\right) \end{aligned} \quad (\text{E-3-1d})$$

whose value would range from 0 to 4 (METRIC1 and 2), 5 (METRIC3), 6 (METRIC4) (from worst to best). Eq. (E-3-1a) is same as the Rank defined in Sect. D-3.

Two sets of calculations were examined, one where the precipitation was given by the MESO GPs and the other using the RAP data. Table E-3-1 shows the verification statistics by RATM for ^{137}Cs deposition. Performance of the revised RATM (Rev. MESO) was significantly improved compared with the preliminary RATM (Pre. MESO) for all rank metrics. The most improvement was obtained in R , which increased from 0.45 in the preliminary version to 0.70 in the revised version. The use of RAP data for precipitation further improved the correlation coefficient to 0.84, while rank metrics became slightly worse due to the deterioration of FB and FOEX. These tendencies in the statistics in the use of RAP data can be understood by the area with high deposition in the northwest of FDNPP and the overestimation of deposition in the west of the Kanto Plain in right panels of Fig. E-3-1; in the aircraft monitoring by MEXT (Fig. 4 of Draxler et al. (2013a)), little or no deposition was observed in the western part of the Kanto Plain.

Table E-3-2 and Fig. E-3-2 show the time evolution and the corresponding statistics for ^{137}Cs concentration at the JAEA-Tokai observation site. Performance of the revised RATM using MESO precipitation was slightly improved in terms of the rank metrics, while the revision did not improve the metrics when the RAP data were used for precipitation. The reason for this deterioration in metrics in the use of RAP data is not obvious, but a similar tendency was also found in the other Task Team's model simulations (Chap. F). Arnold et al. (2015) inferred that the discrepancy of transport patterns by NWP (numerical weather prediction) analyses and the locations of the precipitation may result in a wrong description of the total wet scavenging. The quality of the RAP data itself is also arguable.

Table E-3-1. Statistical metrics for comparison of JMA-RATM simulations with observed deposition pattern of ^{137}Cs using the JAEA source. Bold values indicate best score for each simulation. Reproduced from Saito et al. (2015).

| RATM | R | FB | FA2 (%) | FOEX (%) | FMS (%) | KSP (%) | METRIC 1 | METRIC 2 | METRIC 3 | METRIC 4 |
|-----------|-------------|--------------|--------------|--------------|---------------|-----------|-------------|-------------|-------------|-------------|
| Pre. MESO | 0.45 | -0.02 | 51.01 | -0.46 | 100.00 | 10 | 3.09 | 2.60 | 4.08 | 4.59 |
| Pre. RAP | 0.77 | 0.54 | 41.99 | 9.67 | 100.00 | 11 | 3.22 | 2.63 | 4.02 | 4.44 |
| Rev. MESO | 0.70 | -0.04 | 37.94 | -0.83 | 99.63 | 10 | 3.37 | 2.75 | 4.35 | 4.73 |
| Rev. RAP | 0.84 | 0.56 | 35.73 | 9.12 | 99.08 | 13 | 3.28 | 2.65 | 4.10 | 4.46 |

Table E-3-2. Statistical metrics for comparison of JMA-RATM simulations with observed concentration time series of ¹³⁷Cs at JAEA-Tokai using the JAEA source. Bold values indicate best score for each simulation. Reproduced from Saito et al. (2015).

| RATM | R | FB | FA2 (%) | FOEX (%) | FMS (%) | KSP (%) | METRIC 1 | METRIC 2 | METRIC 3 | METRIC 4 |
|-----------|-------------|--------------|--------------|---------------|--------------|-----------|-------------|-------------|-------------|-------------|
| Pre. MESO | 0.51 | -0.82 | 21.43 | -21.43 | 80.00 | 43 | 2.22 | 1.63 | 2.79 | 3.01 |
| Pre. RAP | 0.59 | -1.66 | 4.76 | -45.24 | 57.50 | 64 | 1.46 | 0.93 | 1.55 | 1.60 |
| Rev. MESO | 0.39 | -0.40 | 14.29 | -19.05 | 77.50 | 43 | 2.30 | 1.67 | 2.92 | 3.06 |
| Rev. RAP | 0.07 | -1.68 | 9.52 | -42.86 | 62.50 | 67 | 1.12 | 0.59 | 1.26 | 1.36 |

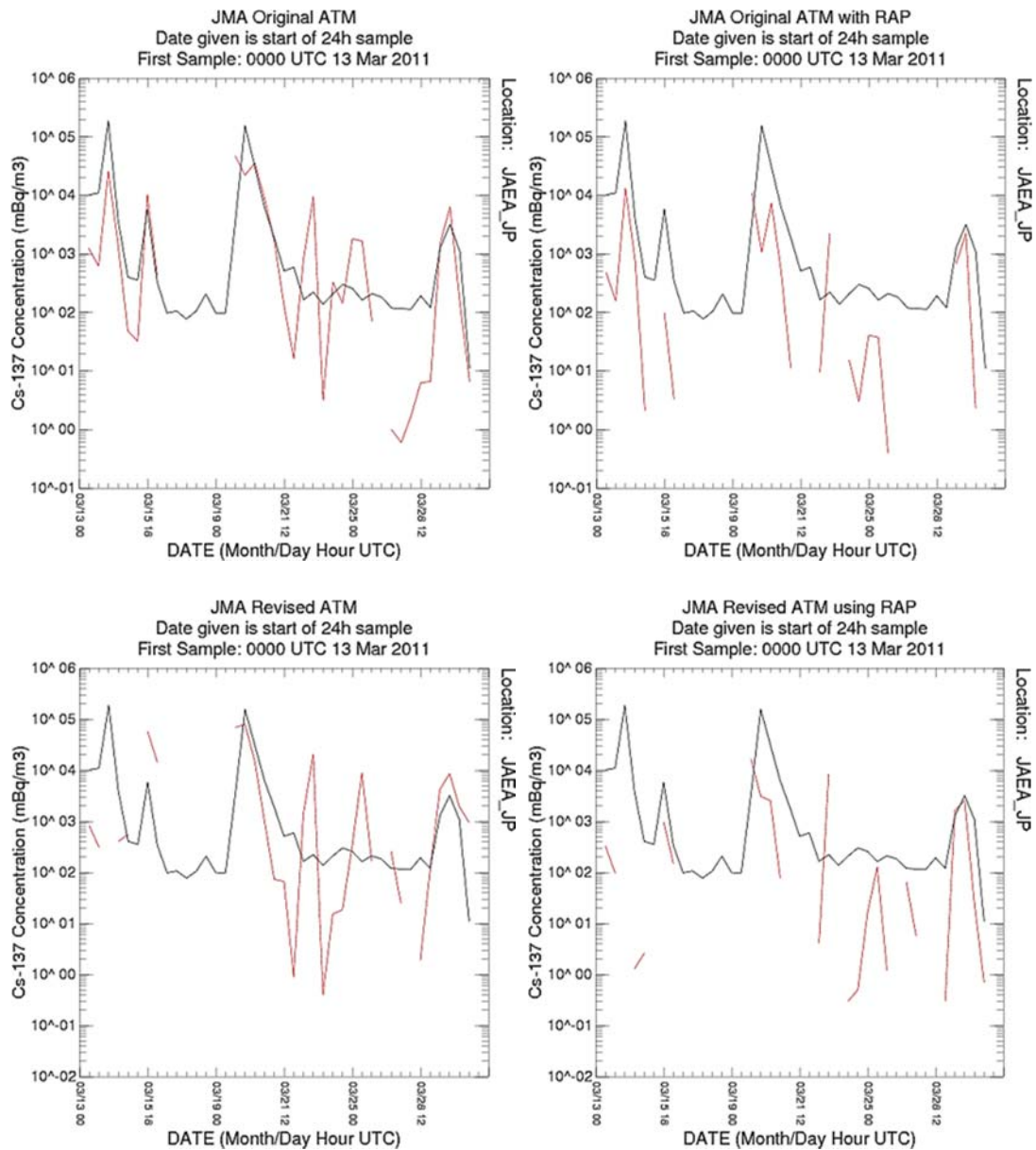


Fig. E-3-2. Same layout as in Fig. E-3-1 but time evolution of ¹³⁷Cs (logarithmic in the ordinate) at JAEA-Tokai for the period 13-31 March 2011. Black lines indicate observation. Red lines show results by the JMA-RATM with the JAEA source estimation. After Saito et al. (2015).

Table E-3-3. Statistical metrics for comparison of JMA-RATM simulations with observed concentration time series of particulate ^{131}I at JAEA-Tokai using the JAEA source. Bold values indicate best score for each simulation. Reproduced from Draxler et al. (2013a).

| RATM | R | FB | FA2 (%) | FOEX (%) | FMS (%) | KSP (%) | METRIC 1 | METRIC 2 | METRIC 3 | METRIC 4 |
|-----------|-------------|--------------|--------------|---------------|--------------|-----------|-------------|-------------|-------------|-------------|
| Pre. MESO | 0.47 | -0.96 | 14.29 | -30.95 | 78.05 | 43 | 2.09 | 1.45 | 2.47 | 2.62 |
| Pre. RAP | 0.67 | -1.71 | 0.00 | -45.24 | 60.98 | 60 | 1.60 | 0.99 | 1.70 | 1.70 |
| Rev. MESO | 0.14 | -0.54 | 16.67 | -23.81 | 75.61 | 40 | 2.11 | 1.52 | 2.63 | 2.80 |
| Rev. RAP | 0.02 | -1.60 | 4.76 | -42.86 | 60.98 | 65 | 1.16 | 0.60 | 1.30 | 1.35 |

Although the bright band is not likely critical in this experiment, radar echoes are scanned around the level of 1 km a.g.l. and solid waters are over-detected in the radar reflectivity. A lower limit of intensity around 0.4 mm h^{-1} is set in RAP, which means that very weak precipitation is not included. As mentioned in Sect. E-1-1, all RAP precipitation was considered to be liquid rain in the wet scavenging calculation in RATM, and this assumption also may yield some errors in the air concentration time evolution. Another possibility is that dispersion of radionuclides to the position of the JAEA site is somewhat uncertain. As suggested in Fig. C-9-7, the southward advection of radionuclides from FDNPP on 15 March 2011 was sensitive to small changes in the wind direction. Therefore, given the inherent limitations in the accuracy of wind direction in meteorological analyses, it may be unrealistic to expect that an RATM can precisely reproduce the time evolution of downwind air concentrations at JAEA-Tokai. In addition, the statistical results may also be affected by remaining uncertainties in the radionuclides release rate estimates which may never be finalized.

Table E-3-3 shows the verification statistics for particulate ^{131}I concentration at the JAEA-Tokai observation site. Similar tendency of the RATM results were confirmed for another type of radionuclides.

c. Sensitivity experiments to RATM parameters

In the revision of RATM, we tested some of the parameters with the greatest uncertainty to determine their impacts on the RATM calculations of the accumulated deposition patterns of ^{137}Cs from 1800 UTC 11 March to 2100 UTC 03 April 2011. A list of values of parameters used in the experiments and corresponding figures are given in Table E-3-4.

(1) Release height

In the WMO Task Teams' experiments, emissions of radionuclides were assumed to be distributed uniformly from the ground to 100 m a.g.l. But this release height may change depending on the atmospheric conditions and situation of the emission. The upper-left panel of Fig. E-3-3 shows the ^{137}Cs accumulated deposition when a lower release height of 30 m is applied. No significant difference was obtained in the dense deposited area compared with the case of the original release height of 100 m (lower-left panel of Fig. E-3-1). A small difference can be seen in the regions with weak deposition

over southern part of the Kanto plain, where the simulated deposition becomes slightly smaller by using the lower release height. This change corresponds to the observed deposition pattern (see Fig. 4 of Draxler et al. (2013a)), and small hotspot northeast of Tokyo is vaguely simulated in this experiment.

(2) Number of computational particles

The upper-right panel of Fig. E-3-3 shows the result when a smaller number of computational particles of 100,000/3 h were employed. Virtually the same result was obtained in the deposition patterns.

(3) Wet scavenging coefficient and application height

Wet scavenging is an important process for the deposition of radionuclides. The middle-left panel of Fig. E-3-3 indicates that when the wet scavenging process is not included in the simulation, the deposition becomes much less compared with the original calculation (lower-left panel of Fig. E-3-1). This result shows that the area with high deposition to the northwest of FDNPP was strongly affected by wet scavenging. However the treatments of scavenging caused by rain and/or snow have many ambiguities. The original version of RATM considered wet scavenging below 3000 m with the scavenging coefficient of Eqs. (E-1-12) and (E-1-13). The middle-right panel of Fig. E-3-3 shows the sensitivity of the results to changes in the below-cloud scavenging coefficient. Here, the scavenging coefficients of Eq. (E-1-13) is replaced by $A = 8.40 \times 10^{-5} \text{ (s}^{-1}\text{)}$, $B = 0.79$, the values used in UKMET-NAME (Table F-2-1). When a larger value is applied, deposition of ^{137}Cs over west of the Kanto Plain is enhanced.

The lower-left panel of Fig. E-3-3 shows the result with the original scavenging application height of 3000 m. A distinct difference from the original simulation is seen over Miyagi prefecture, where overestimation of unobserved deposition is predicted. This result may suggest that the wet scavenging should be confined in lower levels in the case of the FDNPP accident.

(4) Dry deposition application height

Sensitivities to dry deposition surface-layer height and number of computational particles were also examined. Using a lower dry deposition surface layer height $Z_d = 40 \text{ m}$ (the lowest model layer) had little impact on the deposition pattern (the lower-right panel of Fig. E-3-3).

Table E-3-4. List of values of parameters used in the JMA-RATM experiments and corresponding figures.

| Source | Release height (m a.g.l.) | Number of comp. particles (per 3 h) | Time step (min.) | Below-cloud scav. coeff. | | Scav. appl. height (m a.s.l.) | Dry-dep. appl. height (m a.g.l.) | Figures |
|--------|---------------------------|-------------------------------------|------------------|---------------------------------------|---------------------------------------|-------------------------------|----------------------------------|--------------------------|
| | | | | by rain | by snow | | | |
| JAEA | 0-100 | 300,000 | 10 | $A=2.98 \times 10^{-5}$, $B=0.75$ | N/A | <1500 | <100 | low.-left of Fig. E-3-1 |
| JAEA | 0-30 | 300,000 | 10 | $A=2.98 \times 10^{-5}$, $B=0.75$ | N/A | <1500 | <100 | upp.-left of Fig. E-3-3 |
| JAEA | 0-100 | 100,000 | 10 | $A=2.98 \times 10^{-5}$, $B=0.75$ | N/A | <1500 | <100 | upp.-right of Fig. E-3-3 |
| JAEA | 0-100 | 300,000 | 10 | N/A | N/A | N/A | <100 | mid.-left of Fig. E-3-3 |
| JAEA | 0-100 | 300,000 | 10 | $A=8.40 \times 10^{-5}$, $B=0.79$ | N/A | <1500 | <100 | mid.-right of Fig. E-3-3 |
| JAEA | 0-100 | 300,000 | 10 | $A=2.98 \times 10^{-5}$, $B=0.75$ | N/A | <3000 | <100 | low.-left of Fig. E-3-3 |
| JAEA | 0-100 | 300,000 | 10 | $A=2.98 \times 10^{-5}$, $B=0.75$ | N/A | <1500 | <40 | low.-right of Fig. E-3-3 |
| JAEA2 | 0-100 | 300,000 | 10 | $A=2.98 \times 10^{-5}$, $B=0.75$ | N/A | <1500 | <100 | low.-left of Fig. E-3-4 |
| JAEA2 | 0-100 | 300,000 | 5 | $A=2.98 \times 10^{-5}$, $B=0.75$ | $A=2.98 \times 10^{-5}$, $B=0.30$ | <1500 | <100 | low.-right of Fig. E-3-4 |

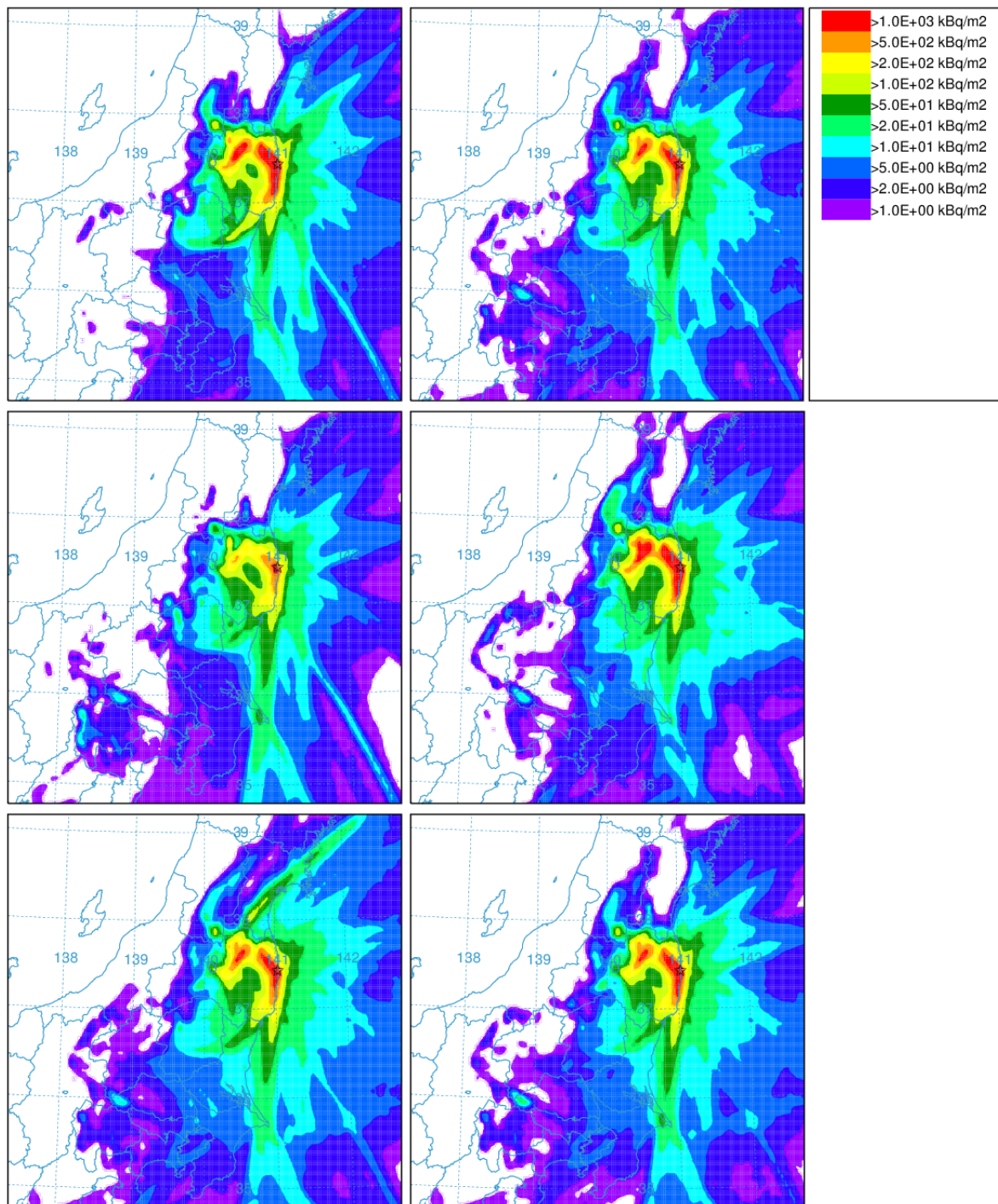


Fig. E-3-3. Same as in the lower-left panel of Fig. E-3-1, but following settings are different: Upper left: for the case with the release height 0-30 m a.g.l. Upper right: for the case with the number of computational particles 100,000/3 h. Middle left: for the case without wet scavenging. Middle right: for the case with the below-cloud scavenging coefficients of $A=8.40 \times 10^{-5} \text{ s}^{-1}$ and $B=0.79$. Lower left: for the case with wet scavenging application height below about 3000 m a.s.l. Lower right: for the case with dry deposition application height less than 40 m. After Saito et al. (2015).

E-3-2. Results of revised RATM for the SCJ Working Group

The SCJ (2014) reviewed the modeling capability of the transport, dispersion and deposition of radioactive materials released to the environment as a result of the FDNPP accident. The primary purpose of this initiative was to assess the uncertainties in the simulation results through model intercomparisons (Sect. G-6). In participating in these model intercomparisons, we used the revised release rate ‘JAEA2’ by Kobayashi et al. (2013) and further modified RATM as mentioned at the end of Sect. E-2.

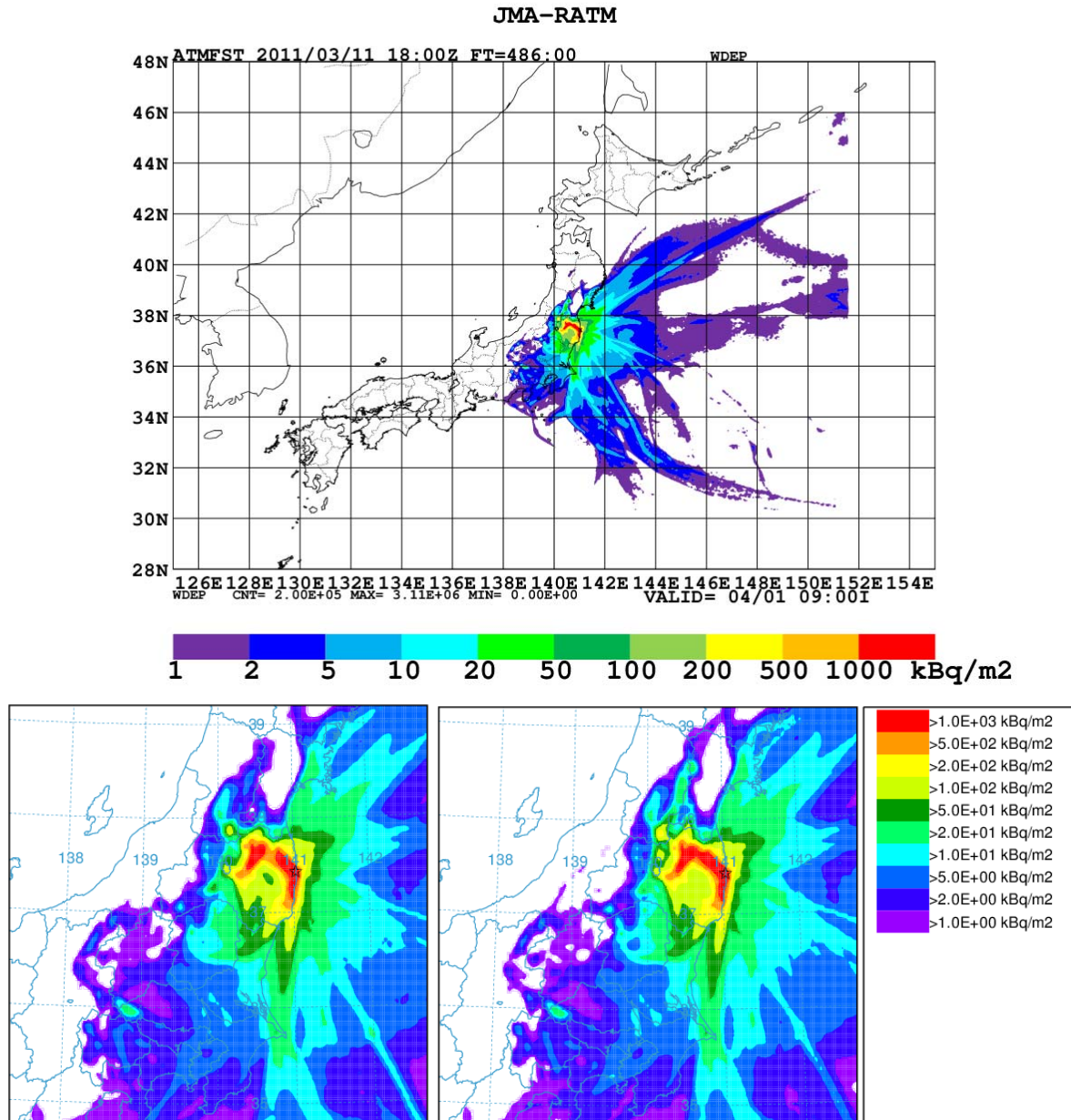


Fig. E-3-4. Upper: distribution of ¹³⁷Cs deposition by JMA-RATM in the SCJ model intercomparison. Lower left: Same as in the lower-left panel of Fig. E-3-1 (below-cloud scavenging is applied only to rain) but for the case that the release rate is given by JAEA2. Lower right: same as in the upper panel but an enlarged view for the same domain as in the lower-left panel of Fig. E-3-1. After Saito et al. (2015).

Figure E-3-4 shows the ^{137}Cs deposition distribution obtained by the SCJ experiment. As seen in its enlarged view (lower-right panel), the area with high deposition northwest of FDNPP is more enhanced relative to the previous RATM results and linked with the hotspot at Naka-dori valley, producing an inverse L-shaped pattern. Because the JAEA2 release rate is somewhat larger than that of JAEA (Fig. 4 of Kobayashi et al. (2013)), the enhancement of deposition was partly caused by the change of the release rate, while the modification of treatment of the wet scavenging (use of solid waters in MESO GPVs) likely contributed to modifying the shape of the area with high deposition. It is noteworthy that in this experiment, a small hotspot in Chiba prefecture (northeast of Tokyo, see Fig. 4 of Draxler et al. (2013a)) is better simulated compared with the previous RATM simulation (the lower-left panel of Fig. E-3-1).

To differentiate the impact of changes to the emission rate and model, we conducted additional experiments. The lower-left panel of Fig. E-3-4 is for the case when only the release rate is changed to JAEA2 source term and with application of below-cloud scavenging only to rain (the same model that in the lower-left panel of Fig. E-3-1). As indicated by these figures, both changes contribute to enhance the inverse L-shaped area with high deposition, but the change of the source term has a larger effect than inclusion of snow in the below-cloud scavenging in terms of the deposition distribution over the Kanto Plain.

E-3-3. Test version of RATM for in-cloud scavenging and future research

Another experiment with in-cloud scavenging for Lpar was conducted to test its impact. In this experiment, the three-dimensional distribution of cloud water analyzed by JNoVA was used to define cloud area and liquid water content. In an analogous form to Eq. (E-1-14), the in-cloud scavenging rate for Lpar is also given by Hertel et al. (1995):

$$\Lambda_r = \frac{0.9}{LWC} \frac{P}{Z_r} [\text{h}^{-1}] \quad (\text{E-3-2})$$

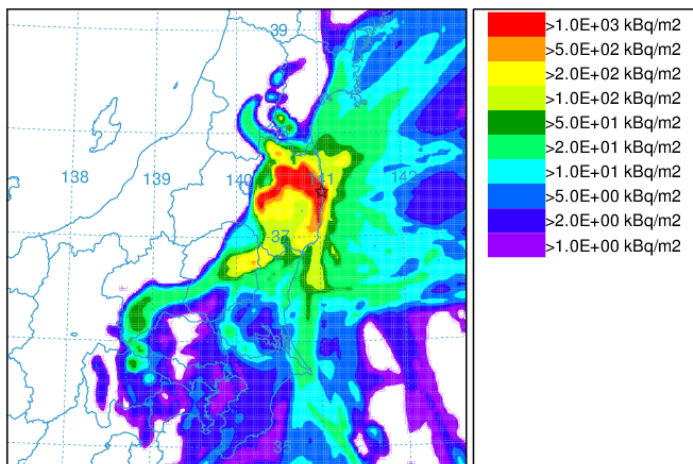


Fig. E-3-5. Same as in the lower-right panel of Fig. E-3-4 but for a test version of JMA-RATM that in-cloud scavenging for Lpar is considered. After Saito et al. (2015).

Figure E-3-5 shows the result when in-cloud scavenging of Eq. (E-3-2) is considered. A very large difference is seen in the north of Kanto Plain. An area with high deposition extends from the eastern part of Fukushima prefecture to west-southwest, resembling the observed hotspot in the northern Kanto Plain (Fig. 4 of Draxler et al. (2013a)). Although the simulated area with high deposition has a small (20-30 km) southward positional lag, this result suggests importance of considering in-cloud scavenging for L_{par} .

In the WMO Task Team and the SCJ Working Group experiments, we used three-hourly MESO analysis as the meteorological field with linear interpolation in time and space to obtain input data for RATM at every 5 or 10 min. time step. The time interval of the meteorological field may not be sufficient to properly treat the upward motion of the radionuclides and to characterize their finer spatiotemporal scale transport due to changes of the wind speed and direction. To obtain more temporally resolved meteorological fields, additional mesoscale model simulations are needed. On the progress of this subject, Sekiyama et al. (2015) conducted the RATM experiments (the same version for SCJ Working Group) using the one-hourly 15 km, 3 km and 500 m NHM-LETKF GPVs (see Sect. G-4).

Use of a lower below-cloud scavenging application height yielded slightly better results in the revised version in some respects, but the same effect could be obtained by reducing the scavenging coefficient itself or changing the source emissions. The results of the additional test of an in-cloud scavenging scheme for L_{par} suggested the importance of its consideration for future model improvements. More sophisticated method should be developed for in-cloud scavenging so that the three-dimensional distribution of rain and snow in the MESO analysis can be used more effectively. In addition, changes of the assumed grain-size distribution and particle density will also have an effect on the surface deposition. These points are all subjects for future research.